Ultrahigh throughput plasma processing of free standing silicon nanocrystals with lognormal size distribution

İlker Doğan,[1,a)] Nicolaas J. Kramer,[1,b)] René H. J. Westermann,[1] Kateřina Dohnalová,[2] Arno H. M. Smets,[3] Marcel A. Verheijen,[1] Tom Gregorkiewicz,[2] and Mauritius C. M. van de Sanden[1,4,c)]

[1]*Department of Applied Physics, Eindhoven University of Technology, P.O. Box 513, 5600 MB Eindhoven, The Netherlands*

[2]*Van der Waals-Zeeman Institute, University of Amsterdam, Science Park 904, 1098 XH Amsterdam, The Netherlands*

[3]*Photovoltaic Materials and Devices Laboratory, Delft University of Technology, P.O. Box 5031, 2600 GA Delft, The Netherlands*

[4]*Dutch Institute for Fundamental Energy Research (DIFFER), P.O. Box 1207, 3430 BE Nieuwegein, The Netherlands*

(Received 1 February 2013; accepted 20 March 2013; published online 3 April 2013)

We demonstrate a method for synthesizing free standing silicon nanocrystals in an argon/silane gas mixture by using a remote expanding thermal plasma. Transmission electron microscopy and Raman spectroscopy measurements reveal that the distribution has a bimodal shape consisting of two distinct groups of small and large silicon nanocrystals with sizes in the range 2–10 nm and 50–120 nm, respectively. We also observe that both size distributions are lognormal which is linked with the growth time and transport of nanocrystals in the plasma. Average size control is achieved by tuning the silane flow injected into the vessel. Analyses on morphological features show that nanocrystals are monocrystalline and spherically shaped. These results imply that formation of silicon nanocrystals is based on nucleation, i.e., these large nanocrystals are not the result of coalescence of small nanocrystals. Photoluminescence measurements show that silicon nanocrystals exhibit a broad emission in the visible region peaked at 725 nm. Nanocrystals are produced with ultrahigh throughput of about 100 mg/min and have state of the art properties, such as controlled size distribution, easy handling, and room temperature visible photoluminescence. [http://dx.doi.org/10.1063/1.4799402]

I. INTRODUCTION

In recent years, prominent features of silicon nanocrystals (Si-NCs) like size-dependent optical and electrical properties, and increased surface reactivity were discovered. Owing to these findings, Si-NCs became not only scientifically interesting but also promising materials for novel applications. For instance, Si-NCs can potentially be used as tunable light emitters in light emitting devices,[1] charge storage elements in high capacity Li-ion batteries[2] and non-volatile memories,[3] and spectrum converters in next generation solar cells for higher efficiency.[4] In the context of future applications with Si-NCs, realizing efficient and reliable devices by using scalable and low-cost techniques is of critical importance. Therefore, main research challenges of Si-NC synthesis are size control, surface engineering, easy handling, and high throughput processing.

In the literature, several Si-NC synthesis methods have been reported. Sputtering is convenient for synthesizing size controlled and luminescent Si-NCs.[5,6] A drawback of this technique is the low processing rate, hampering large scale applications of Si-NCs using this technology. Formation of Si-NCs is only favorable with intensive heat treatments. Moreover, Si-NCs are embedded in a matrix and handling of nanocrystals is difficult. Ion implantation is another method for synthesizing Si-NCs.[7,8] In this technique, the projected range of implanted ions has a dispersed density profile. During annealing, therefore, a size distribution of Si-NCs is obtained. Similar to the sputtering, the processing rate is low and handling of Si-NCs is not feasible. Apart from these techniques, a variety of chemical solution-based production methods of Si-NCs have been reported in the literature. Such Si-NC synthesis techniques include using inverse micelles as reaction vessels,[9] reduction of silicon halides,[10] and thermal degradation of phenyl-silane groups at high temperatures and pressures.[11] These techniques produce free standing Si-NCs. However, most of these techniques require multiple production steps and have low yields. Somewhere in between the physical and chemical processing techniques are gas phase or plasma based synthesis techniques. Gas phase synthesis of Si-NCs by means of high power infrared laser pyrolysis produces free standing Si-NCs with better size control and relatively higher throughputs.[12] Yet, manipulation of Si-NCs could be a problem as nanocrystals coagulate strongly. This can detrimentally affect the unique properties of produced Si-NCs. Therefore, utilizing this technique, an etching route for separation of coagulated nanocrystals might be necessary.[13] In contrast, using plasmas for production of silicon nanocrystals has many advantages. Plasmas offer more flexibility on size control and surface passivation

[a)]Electronic mail: i.dogan@tue.nl
[b)]Present address: Department of Mechanical Engineering, University of Minnesota, Minneapolis, Minnesota 55455, USA.
[c)]Electronic mail: m.c.m.vandesanden@differ.nl

during synthesis. Particle charging in the plasma inhibits strong coagulation of synthesized Si-NCs and enables easy handling. Non-thermal plasmas are reported as being suitable for synthesizing free standing Si-NCs by using various precursors.[14,15] Moreover, *in situ* passivation of Si-NCs with chlorine[14] and hydrogen,[15,16] and *in situ* etching[17] is possible. When compared to the techniques mentioned above, non-thermal plasmas have higher deposition rates with better size control and could be considered as a next step in the context of large scale production. However, achieving the required throughputs for industrial applications is still a problem due to scalability issues of that non-thermal plasma technology in view of the usual low gas flow used. Thus, a higher throughput, with better compatibility of the processing tool to industry, is necessary.

A suitable and scalable plasma technique is the remote expanding thermal plasma (ETP). ETP is a remote plasma in the sense that plasma production, plasma transport, and surface treatment regions are geometrically separated.[18] Consequently, downstream properties, in the region where plasma transport and Si-NC formation take place, have no influence on the upstream plasma production region. This enables independent variation of processing parameters (i.e., pressure, plasma power, substrate conditioning), thus simplifying optimization of the quality and processing rate of the material to be synthesized. Apart from that, utilizing high power and high feed gas flows injected into downstream promote high throughput processing of silicon based thin films. Solar grade hydrogenated amorphous silicon (a-Si:H)[19] and silicon nitride (a-SiN_x:H)[20] thin films have been reported at deposition rates up to 10 nm/s in the optimized parameter regime. In addition to silicon based thin films, realization of silicon based nanomaterials by using the ETP is possible. In particular, higher densities of silane related species can initiate gas phase polymerization reaction sequences realizing formation of small molecular clusters. Within the residence time of the plasma, these clusters can reach significant sizes.

Inspired by this idea, we realize the use of the ETP for producing free standing Si-NCs in an argon plasma with various downstream injected flow rates of silane. Formation of primary ionic silicon clusters is favored by means of silane polymerization reactions in which recombining interactions of ions, neutrals, and silane molecules are involved.[21] Primary ionic silicon clusters that reach a critical stable size and number density in the plasma grow further via nucleation.[22] The required high temperature for crystallization during the growth is reached by means of growth reactions and ion recombination on the nanocrystal surface,[23] and hydrogen-hydrogen association since the removal of surface hydrogen atoms by the atomic hydrogen is an important heating mechanism.[24] The final size of Si-NCs is determined by the time in the plasma during which the nucleation takes place.[25] Indeed, we find an ultrahigh processing rate of Si-NCs under optimum parameter regime about 100 mg/min. Synthesized Si-NCs have a bimodal size distribution that suggests the presence of two distinct residence times in different plasma regions. Apart from that, observed size distributions are lognormal. As we will demonstrate, no evidence is found for coalescence of smaller nanocrystals into larger particles as large particles have monocrystalline morphology. Size distribution of small Si-NCs is controlled by tuning the silane flow rate.

This paper reports the formation mechanism and material properties of Si-NCs synthesized in argon/silane gas mixtures by using the ETP. Section II is devoted to a molecular level description on the formation mechanism of Si-NCs. In Sec. III, the experimental details are provided. In Sec. IV, we show the morphological properties and size distribution of Si-NCs acquired by using X-ray diffraction (XRD), transmission electron microscopy (TEM), Raman spectroscopy (RS), and photoluminescence (PL) spectroscopy. Finally, important aspects, advantages, and challenges of this technology are summarized.

II. FORMATION OF SILICON NANOCRYSTALS IN EXPANDING THERMAL PLASMA

Formation of nano-sized silicon particles is observed and extensively studied in various plasmas.[14,15,26–29] In addition to silicon, nanoparticles of germanium,[30] silicon carbide, and carbon[31] can be synthesized in plasmas depending on the feed gases used. Up to now, several models are developed to describe the growth mechanism of nanoparticles.[32–35] All these models have in common that nanoparticle growth starts with initial polymerization reactions, induced by radicals or ions, leading to formation of primary ionic clusters. Growth of particles is favorable when the primary ionic cluster reaches a critical size of about 1–2 nm.[29] After reaching the critical size, the probability of reactive gas phase species nucleating on the cluster surface becomes higher than the probability of diffusion losses.[36] Eventually, rapid nucleation and agglomeration takes place leading to formation of particles with sizes from a few to hundreds of nanometers as long as the residence time for growth reactions permits.[25] Depending on the plasma technique used, these clusters can be neutral or positively/negatively charged during the growth. Once the particles are formed, they are influenced by various forces in the plasma, such as the electric field force, ion and neutral drag force, and thermophoretic force, potentially providing longer residence times than provided by feed gas flow and pumping speed. A particular example of this latter effect is the confinement of negatively charged particles in RF capacitively coupled plasmas.[27] Similar longer residence times of particles can be provided by confined recirculation cells in plasma chemical reactors.[37]

Before discussing the particular plasma chemistry of Si-NC formation in the ETP, the flow pattern inside the reactor needs to be briefly discussed. In Fig. 1, the ETP reactor is schematically shown. An argon plasma, having temperatures of around 1 eV and an ionization degree of about 10%, is generated inside a cascaded arc at subatmospheric pressures. The overall 2D flow simulation of the plasma is also shown in Fig. 1. To obtain the picture of the flow, Navier-Stokes equations are numerically solved with no slip boundary conditions at the walls,[37] a parallel flow with parabolic velocity distribution with $U_0 = 900$ m/s at the arc exit, i.e., where the argon gas enters the vessel. This plasma expands

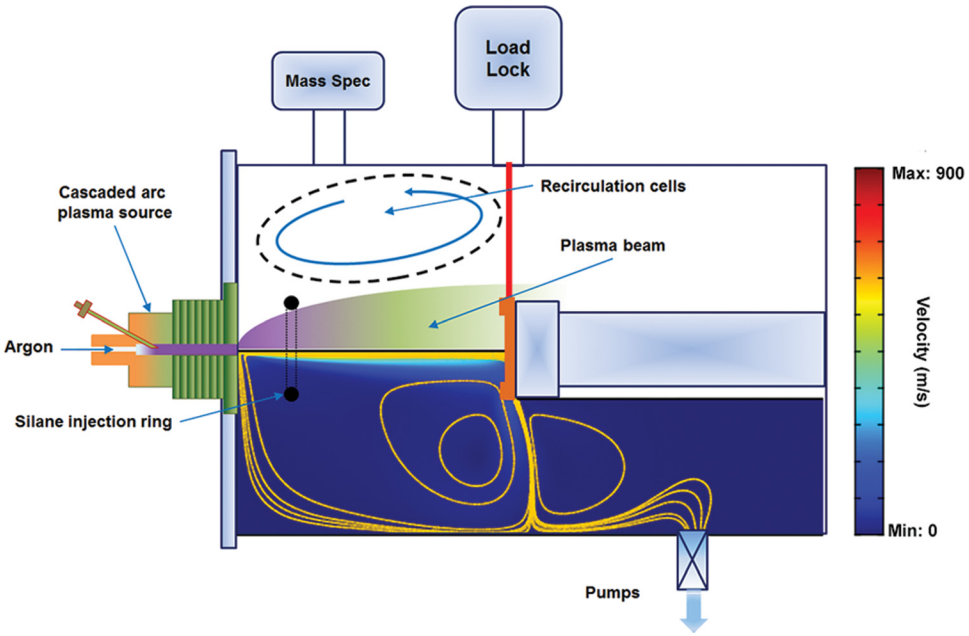

FIG. 1. The expanding thermal plasma, which is used for synthesizing Si-NCs. Two dimensional velocity simulation of the pure argon plasma expansion is also shown (bottom half of the image). The plasma expands in the form of a beam surrounded by recirculation cells as evidenced from closed stream lines.

supersonically into a low pressure vessel, where after a stationary shock front located 3 cm in front of the nozzle,[37] it expands further subsonically towards a temperature controlled substrate. Due to the finite pumping capacity, recirculation cells are formed in the background of the plasma beam. It should be noted that this flow geometry of the ETP and its remote character result in a flow dynamics in which the residence time in the plasma beam τ_{beam} is relatively short (the residence time within the plasma beam depends on the axial velocity and the distance between the plasma source and substrate) and the residence time in the recirculation cells is τ_{recirc} relatively long. As the recirculation cells consist of closed stream lines,[37] transport between regions of open stream lines (which end at the pumps and which encompass the plasma beam) and closed stream lines occurs by diffusion. This results in much longer residence times of particles in the recirculation cells than the overall residence time τ_{res} calculated on basis of the injected total flow, reactor volume, and pumping capacity. The following scaling holds

$$\tau_{beam} \ll \tau_{res} < \tau_{recirc}, \tag{1}$$

where $\tau_{beam} \leq 10$ ms and $\tau_{recirc} \sim 0.1$–0.5 s as determined from mass spectroscopy measurements.[38]

Previous studies on the ETP have demonstrated the observation of small ionic Si clusters in a configuration where the arc operated in a pure argon/hydrogen plasma and silane gas was injected in the expanding beam in the downstream region.[21,39] Mass spectroscopy experiments in silane/argon/hydrogen plasmas have demonstrated the presence of hydrogen-poor cationic clusters up to ten silicon atoms, limited by the range of the mass spectrometer.

In this work, we use an argon/silane plasma for synthesizing Si-NCs. Due to the remote feature of the expanding DC plasma, the electron temperature is relatively low ($T_e \sim 0.1$–0.3 eV) in the downstream region, and therefore, the plasma chemistry is ruled by Ar^+ ions that are produced in the cascaded arc. Produced Ar^+ ions initiate dissociative charge exchange reactions with silane molecules leading to the formation of SiH_n^+ ($n \leq 3$) ions

$$Ar^+ + SiH_4 \rightarrow SiH_n^+ + lH + mH_2 + Ar, \tag{2}$$

with $n \leq 3$ and $l + 2m + n = 4$. The rate of this reaction is on the order of $k \sim 10^{-16}$ m^3 s^{-1}.[38] The molecular ion formed in Eq. (2) can further react with an electron by means of a dissociative recombination reaction

$$SiH_n^+ + e^- \rightarrow SiH_p + lH + mH_2, \tag{3}$$

with $n \leq 3$, $p \leq 2$, and $n = p + l + 2m$. The rate of dissociative recombination shown in Eq. (3) depends on the electron temperature ($k \sim 10^{-13}\, T_e^{-1/2}$ m^3 s^{-1}, T_e in eV)[24] and for the ETP downstream, the rate is in the range of 1.5–3.0×10^{-13} m^3 s^{-1}. The radicals formed in this way can undergo further polymerization reactions with silane to form polysilanes, e.g.,

$$SiH_2 + SiH_4 \rightarrow Si_2H_6^* \rightarrow Si_2H_5 + H, \tag{4}$$

and eventually larger clusters. The rate is 4.6×10^{-16} m^3 s^{-1} for this reaction.[24] Another pathway of the molecular ions formed in Eq. (2) is to react with silane (or the polysilane clusters formed) in an associative charge exchange reaction with a rate of $k \sim 6.0 \times 10^{-16}$ m^3 s^{-1},[24] leading to formation of polysilanes ions via ion-molecule reactions, e.g., for SiH_3^+

$$SiH_3^+ + SiH_4 \rightarrow Si_2H_5^+ + H_2 \tag{5}$$

with the general form

$$Si_nH_{2n+1}^+ + SiH_4 \rightarrow Si_{n+1}H_p^+ + lH + mH_2, \tag{6}$$

where $2n + 5 = l + 2m + p$. Since the rate of dissociative recombination is three orders of magnitude faster than

ion-molecule reaction rate, the radical pathway is dominant until the electron density is quenched to values where the electron to ion density ratio is approximately greater than 10^{-3}. After this point, the ion-molecule route becomes dominant.

In both of these radical and ion assisted routes, addition of further species drives the polymerization process. As a result, first ionic clusters with a few silicon atoms appear in the plasma. When approximately 30 silicon atoms have come together to form a cluster, the critical size ($\sim$1 nm) is reached. Considering the partial silane pressures used in this work with respect to our previous work,[38] this is easily achieved in times much shorter than the residence time in the plasma beam. Ionic clusters larger than the critical size can be considered as stable Si-NCs as they survive in the plasma and grow further via vapor growth, i.e., nucleation of silane molecules and radicals on the cluster. During nucleation, the abundant atomic hydrogen produced in the plasma (atomic hydrogen in Eqs. (2) and (3)) can undergo hydrogen abstraction reactions with Si_nH_m radicals and $Si_nH_m^+$ ions

$$H + Si_nH_m \rightarrow Si_nH_{m-1} + H_2, \quad (7)$$

$$H + Si_nH_m^+ \rightarrow Si_nH_{m-1}^+ + H_2. \quad (8)$$

As these are exothermic interactions,[40] the heat released from these reactions can be considered as an important crystallization mechanism of silicon nanoparticles during growth.[24] Other possible crystallization mechanisms are the excess energy released by the collisional stabilization of excited $Si_nH_m^*$ species (Eq. (4)) and ion recombination on the nanocrystal surface.[23]

In the early stages of nucleation (particle sizes $\sim$1–2 nm), most of the particles are found to be neutral[41] or even positively charged[21,38] due to the Ar^+ ion induced chemistry. Because of this reason, the electric field force has a minor effect on the transport of particles in the plasma. Therefore, in the ETP, the main force acting on Si-NCs is by means of the flow field, i.e., in the downstream region, Si-NCs follow the trajectories dictated by the drag force. For Si-NCs diffused into recirculation cells, the motion is driven by the centrifugal force where the flow field dictates a closed loop. As a matter of fact, the influence of flow fields overtakes the weak repulsive forces between oppositely charged Si-NCs preventing sticking and coagulation. Thus, particle growth dominantly proceeds via nucleation. The absence of any grain boundaries in large Si-NCs as observed from HRTEM images is an evidence for the fact that large Si-NCs are not the result of coagulation of smaller Si-NCs but that each Si-NC is the result of crystal growth upon a nucleation event starting from a primary core cluster. As expected, the characteristic shape of the final size distribution of nanocrystals is influenced by the transport of species and nanoparticles in the plasma. According to a particle nucleation model,[25] in systems where particles are transported through a finite-length growth zone by means of diffusion and drag, a lognormal particle size distribution should be expected. In this model, the origin of the lognormal distribution is explained based on the nucleation event during particle growth. Lognormal distributions of metal and semiconductor nanoparticles are experimentally observed in various nanoparticle synthesis methods.[42,43] Analyses on size distributions of Si-NCs synthesized in the ETP demonstrate that Si-NCs formed in the central beam and in the recirculation cells have lognormal size distributions. Moreover, the observation of a single crystalline morphology of Si-NCs correlates well with the theory in which the particle formation mechanism is based only on nucleation.[25]

III. EXPERIMENT

The expanding thermal plasma consists of two main parts as shown in Fig. 1: a cascaded arc for generating the thermal plasma, and a cylindrical low pressure downstream vessel for synthesizing and depositing Si-NCs. Three cathodes are used for igniting the plasma in the arc channel which has a diameter of 4 mm. The structure of the arc is a combination of water cooled, electrically floating copper plates. Argon gas is introduced into the arc at a fixed flow rate of 20 sccs (standard cubic centimeters per second). The DC discharge is controlled by means of the current level and is held at 45 A during experiments. The voltage on each cathode is in the range of 30–40 V, leading to plasma powers in the range 1.3–1.8 kW. The pressure in the arc is in the range of 150–200 mbar. The thermal plasma generated in the arc channel has an electron and gas temperature of about 1 eV (Ref. 44) and an electron density of $n_e \sim 10^{22}\,m^{-3}$.[38] The downstream deposition chamber is pumped down to a pressure of 1 mbar. The plasma density in the downstream is about 10^{21}–$10^{22}\,m^{-3}$.[45] Silane is introduced as the reactive gas by means of an injection ring, which is placed in the subsonic region, 5 cm in front of the nozzle exit. The injection ring has a diameter of 8 cm and has eight holes each 1 mm in diameter. Silane flow is varied in the range 1–10 sccs. The gas temperature at the injection point is about 1500 K and decreases rapidly to 400 K in the vicinity of substrate and in recirculation cells.[37] Si (100) wafers and plexiglass substrates are transferred into the deposition vessel from a load lock by means of a magnetic arm. The substrate holder is protected by a shutter during the startup of the plasma. The distance from the nozzle to the substrate holder is 40 cm. A list of setup parameters is given in Table I.

X-ray diffraction data are obtained by a diffractometer using Cu K_α radiation. 2θ scans are recorded in the range 20°–60° for observation of the morphology of Si-NCs. The (111) diffraction peak of crystalline silicon is analyzed for

TABLE I. Setup parameters for the expanding thermal plasma.

Parameter	Processing values
Ar flow	20 sccs
SiH_4 flow	1–10 sccs
Arc current	45 A
Arc voltage	30–40 V
Arc pressure	0.1–0.2 bar
Vessel pressure	1.0 mbar
Substrate temperature	25 °C
Process time	5 s

average nanocrystal size estimation. Transmission electron microscopy is performed after transferring the deposited material to holey carbon films. Beam intensities at 300 kV accelerating voltage are chosen sufficiently low in order to prevent any electron-beam related artifacts on Si-NCs. Raman spectroscopy measurements are done with a 514 nm laser. The step size of the measurement is 1.7 cm^{-1}. The laser power during the measurements is fixed at 0.3 W/mm^2 with a spot size of approximately 400 μm^2. This laser power is sufficiently lower than the threshold power for Fano broadening,[46] which is an artificial broadening and shift observed in the Raman spectrum of Si-NCs as a result of laser induced heating. By means of a power series experiment, it is also verified that the selected laser power does not induce any artificial shift and broadening in the Raman spectrum of Si-NCs. Observed Raman spectra are deconvoluted for estimation of the nanocrystal size distribution by using Lorentz and lognormal fitting functions. PL measurements are done by illuminating the samples using a 334 nm Ar laser with continuous mode. Luminescence is detected with a UV-grade fiber, connected to a spectrometer, coupled to a nitrogen cooled CCD.

The processing rate of synthesized Si-NCs defined as weight/time is obtained by measuring the weight of the deposits after the deposition. The processing rate of Si-NCs is measured about 100 mg/min for various silane flow rates injected downstream. Fig. 2 shows an image of the deposited Si-NCs on a 4 in. Si (100) wafer indicating three different deposition areas namely, central, ring, and outer regions. This pattern of deposition is closely related to the flow of Si-NCs in different plasma regions. The yellow colored ring-like feature with eight edges is a result of the trajectory of the injected silane from the injection ring. The central and outer parts are the deposits under the influence of the plasma beam and recirculation zones, respectively. Since Si-NCs with different sizes diffuse randomly between the reactor regions, nanocrystals are expected to have a mixed size distribution for each position on the substrate. Therefore, in all of the measurements, only data from the central parts are compared for better consistency unless otherwise indicated.

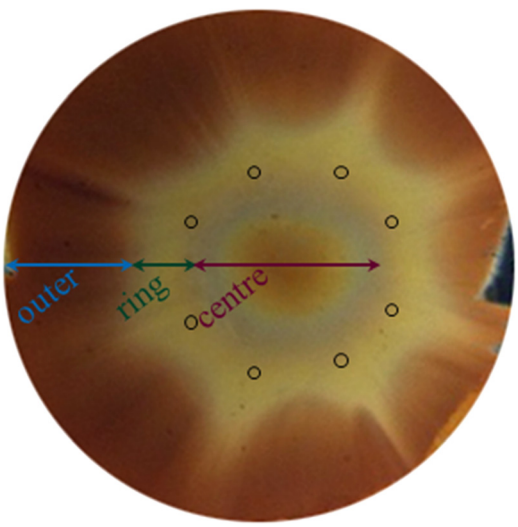

FIG. 2. Image of as-deposited Si-NCs on a 4 in. substrate. Three main regions are recognized: a central part, a ring part, and an outer part. This pattern is imposed by the flow field in the downstream region which affects the transport of Si-NCs. Nanocrystals are deposited on the whole substrate surface; however, because of its well defined shape, the central part is analyzed for nanocrystal properties and for comparison of the data.

IV. RESULTS AND DISCUSSION

A. X-ray diffraction

XRD is used for obtaining information about the morphology, i.e., the crystallinity and average size of Si-NCs synthesized in the ETP. XRD spectra of Si-NCs as a function of silane flow rate are demonstrated in Fig. 3. From the spectra, three diffraction peaks corresponding to Si (111), (220), and (311) crystal planes are observed at diffraction angles 28.4°, 47.3°, and 56.2°, respectively. The spectra do not show any amorphous feature as noticed from the flat background signal. The increase of XRD intensity with silane flow under identical measurement conditions is a sign of an increased amount of deposited material. Apart from that, observed (111) peaks of Si-NCs at 28.4° indicate that Si-NCs are under minimal tensile strain as $2\theta = 28.4°$ is the Si (111) peak in unstrained polycrystalline Si.[47] Strain free feature of Si-NCs produced in the ETP is most probably related with the absence of a solid host matrix which can induce strain as a result of lattice mismatch. Fig. 4(a) shows Si (111) diffraction peaks analyzed for average size estimation of Si-NCs by using the Pseudo-Voigt fitting function. The average crystal size is calculated using Scherrer's formula,[48] posing that the diffraction peak width is inversely proportional to the crystal size

$$D = \frac{K\lambda}{\beta(2\theta)\cos\theta}. \tag{9}$$

In Eq. (9), D is the average crystal size, K is the Scherrer constant (~0.9 for spherical nanoparticles), λ is the wavelength of the X-ray (1.54 Å for Cu K_α), $\beta(2\theta)$ is the FWHM in radians, and θ is the position of the diffraction peak. The average crystallite size of Si-NCs varies in the range of

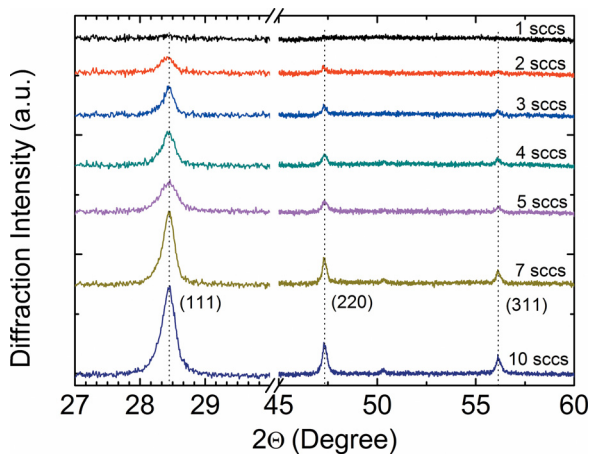

FIG. 3. XRD spectra of Si-NCs as a function of silane flow rate. Three diffraction peaks are observed corresponding to the Si (111), (220), and (311) reflections. The absence of a background signal is an indication of good crystallinity.

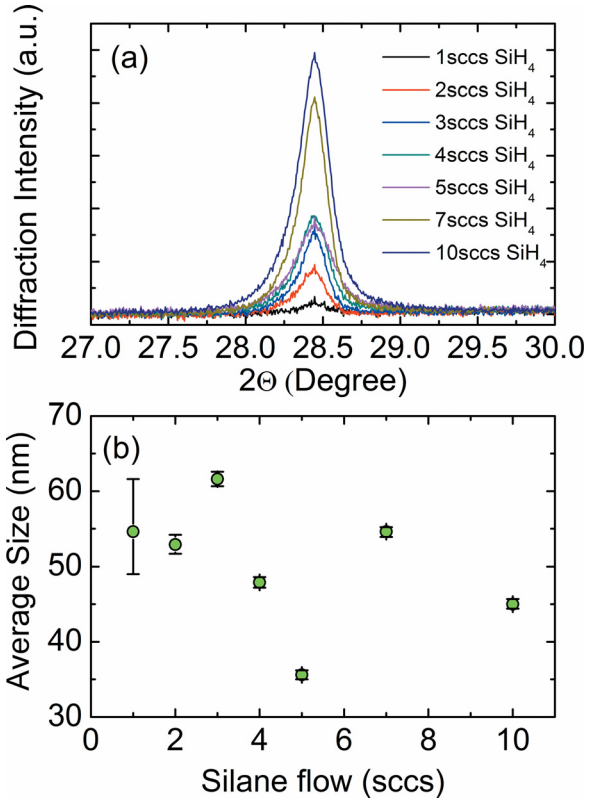

FIG. 4. Si(111) diffraction peaks as a function of silane flow rate. The FWHM of the peaks is used for calculation of the average crystallite size (a). Average crystallite size as a function of silane flow rate as determined by using Scherrer's formula (b).

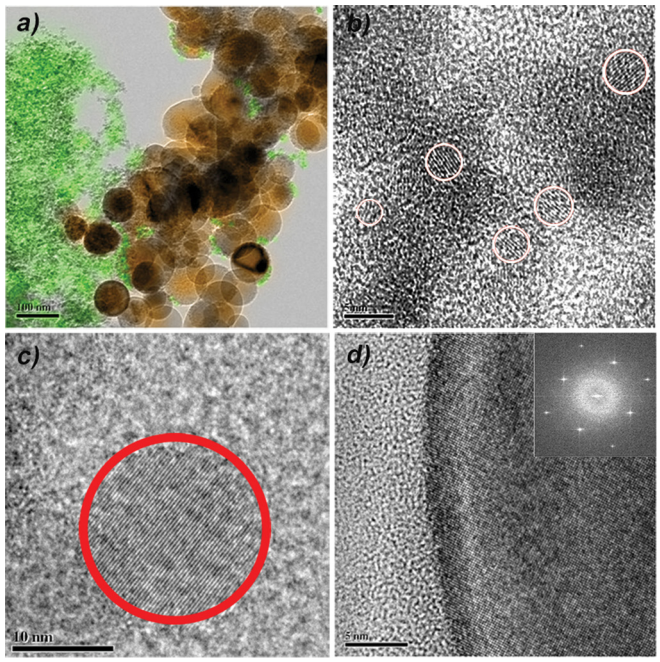

FIG. 5. TEM images displaying a bimodal size distribution of free standing, spherical Si-NCs. Green color: small Si-NCs. Brown color: large Si-NCs. Colors do not mention a scale (a). Small Si-NCs with sizes of about 4 nm (b) and 10 nm (c). Detail from a large Si-NC with a size of about ~80 nm with a fast Fourier transform (FFT) image (inset) demonstrating its crystalline morphology (d). All images are taken from a sample synthesized with 4 sccs silane flow rate.

35–60 nm, as shown in Fig. 4(b). Here, lack of a clear trend in size with silane flow rate should be interpreted carefully. First of all, the calculated crystal sizes correspond to the average size distribution of Si-NCs and no information can be obtained about the sub-distributions. Second, the characteristic lognormal shape of the sub-distributions cannot be probed. Thus, although providing valuable information on the crystallinity of Si-NCs, XRD is insufficient for facilitating a detailed size analysis of nanocrystals with a multimodal size distribution. In this case, a more sensitive technique for analyzing the size distribution is needed.

B. Transmission electron microscopy

For getting more information on the size distribution, shape, and arrangement of Si-NCs, TEM is used. Fig. 5 shows a series of TEM images of the sample deposited with 4 sccs silane flow rate. The image shown in Fig. 5(a) depicts a random mixture of Si-NCs. With Fig. 5(a), we draw attention to three important points. First of all, most of the Si-NCs visible in the image are spherically shaped and have a monocrystalline morphology. Second, Si-NCs are observed as free standing. Third, Si-NCs do not have one distinct size. In fact, there is a bimodal size distribution. In other words, Si-NCs are divided into two main groups with respect to their size. The first group is composed of small Si-NCs with sizes in the range of 2–10 nm, and the second group consists of larger Si-NCs with sizes in the range of 50–120 nm. HRTEM images of Si-NCs are acquired to obtain more detailed information about their crystallinity. Fig. 5(b) shows a group of small Si-NCs with sizes of about 4 nm, while Figs. 5(c) and 5(d) show individual Si-NCs with sizes of about 10 nm and 80 nm, respectively. It should be noted that all images show defect-free Si crystal lattices without any dislocations or grain boundaries, implying a uniform and monocrystalline character of all Si-NCs. This observation shows that particle growth occurs by means of nucleation instead of coagulation. The monocrystalline particle morphology also suggests that sufficient heat is available for heating the particles up to crystallization temperatures. As discussed above, the heat is most probably provided by abstraction and adsorption reactions of silane molecules and hydrogen radicals.

The Si-NC size distribution is investigated in more detail by statistical size distribution studies. Fig. 6 plots the variation of Si-NC sizes in terms of count frequency obtained from TEM images (approximately 200 NCs are counted from the sample shown in Fig. 5(a)). The measurements show the bimodal size distribution of Si-NCs. An interesting feature of Fig. 6 is that the size distribution of small Si-NCs is narrow and mostly in the range 4–5 nm. In contrast, a wider size distribution of large Si-NCs is obtained from 50 to 120 nm. Remarkably, the size distribution of small and large Si-NCs exhibits a lognormal behavior suggesting that these nanocrystals are influenced by diffusion and drag forces during nucleation.[25] An important point to note here is the difficulty of accurately measuring the diameter of the smaller Si-NCs. Resolving small Si-NC is a challenging task since all analyzed samples are densely populated and most of the small Si-NCs are found as large

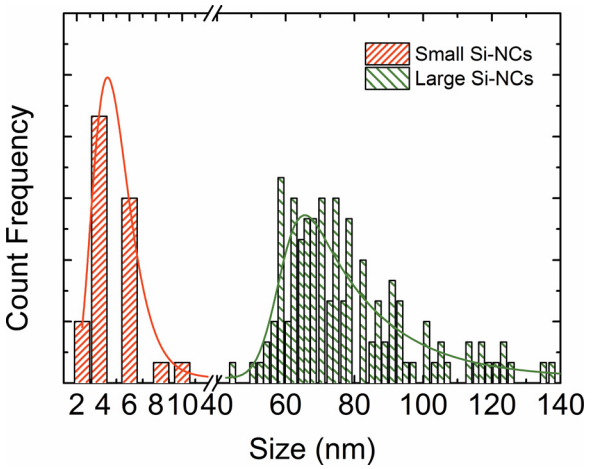

FIG. 6. Statistical size distribution of Si-NCs deposited with 4 sccs SiH_4 flow, based on the size measurements performed using TEM images. Approximately 200 Si-NCs are counted for generating the image.

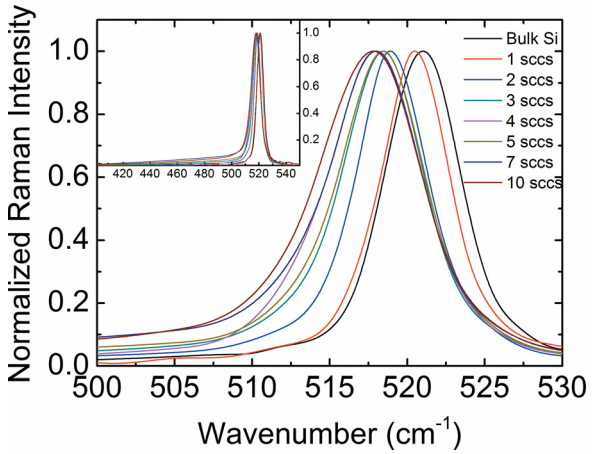

FIG. 7. Normalized Raman spectra of Si-NCs for various SiH_4 flow rates. Inset: Wide-range spectra from 400 to 550 cm^{-1} demonstrating the absence of amorphous features. Plexiglass substrates are used in this experiment to make sure that the observed signal is purely from the deposited material.

groups attached together and/or attached on the large Si-NCs. For this reason, only the small Si-NCs that could be imaged separately are used in the analysis. This leads to an underestimation of the relative number of small Si-NCs. However, the result shown in Fig. 6 provides useful information about the behavior of the size distribution in the deposited samples.

C. Raman spectroscopy

A sophisticated technique for the analysis of the morphology and size distribution of Si-NCs is Raman spectroscopy. RS has major advantages over XRD and TEM. First of all, amorphous and crystalline features of silicon could be independently detected and analyzed since a-Si and c-Si have their own characteristic phonon frequencies. Second, size related effects are not only observed by peak broadening, but also detected by a shift to lower wavenumbers from the transverse optical (TO) phonon mode of bulk silicon located at 521 cm^{-1}. This effect is known as the phonon confinement effect, which describes the confinement of phonons in the grain boundaries due to reduced size.[49–52] For Si-NCs, effects of phonon confinement are generally significant when the size of the nanocrystal is smaller than 20 nm.[52] For larger Si-NCs, the peak position remains unchanged at 521 cm^{-1}; however, a negligible broadening of the TO mode is observed with respect to the natural Lorentzian line shape of bulk silicon. Fig. 7 demonstrates the normalized Raman spectra of Si-NCs as a function of silane flow rate. The inset shows wide-scan spectra. The presence of strong TO phonon modes and the absence of amorphous silicon related modes, i.e., a broad peak centered at 480 cm^{-1}, indicate that the synthesized material is predominantly crystalline. From the spectra, a clear shift to lower wavenumbers and a broadening of the Raman peak with increased asymmetry is observed with increasing silane flow rate. Moreover, the high frequency tails of the phonon peaks do not depart significantly from its actual position while the low frequency tails shift significantly. This observation is consistent with the presence of a bimodal size distribution since the distribution of small Si-NCs exhibits a shift to lower wavenumbers while large Si-NCs are still present in the mixture. Therefore, contributions from small and large Si-NCs can be estimated by deconvolution of the observed spectra. Fig. 8(a) shows the deconvoluted spectrum of Si-NCs synthesized with 4 sccs silane flow rate. The distribution of large Si-NCs is defined by a Lorentzian peak located at 521 cm^{-1}. Since we observe a lognormal size distribution from statistical studies, the remaining part of the spectrum is defined by a phonon confinement model, which involves a lognormal distribution function for representing the size distribution of small Si-NCs.[49] The asymmetry of the lognormal shape is a result of

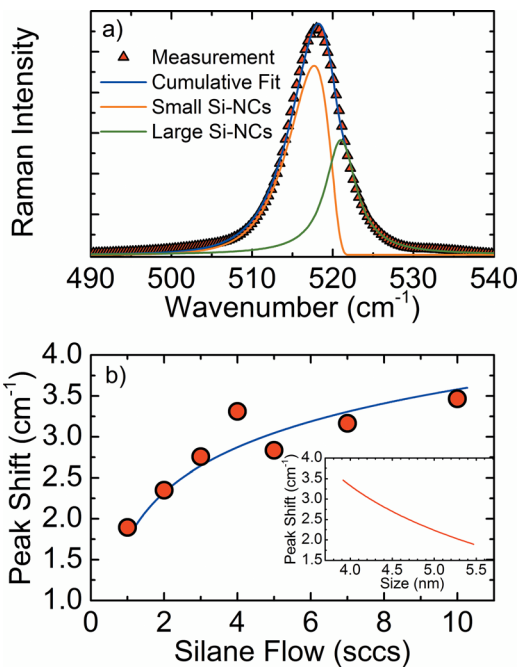

FIG. 8. A deconvoluted Raman spectrum of Si-NCs demonstrating separate contributions from small and large nanocrystals. The sample deposited with 4 sccs silane flow rate is shown (a). The peak shift and peak size (inset) of small Si-NCs as a function of silane flow rate. Inset data are plotted according to the analytical formula (Ref. 49) based on the phonon confinement model (Ref. 52) (b). Peak deconvolution routes are performed in the same way as shown in (a).

size distribution, and the maximum of the peak corresponds to the peak size. The shift of the peak position from the bulk silicon TO phonon mode is used to estimate the average size of small Si-NCs by using the size related shift formula[49]

$$\Delta\omega(D) = \frac{120.8}{\frac{a}{D} + 0.53} \times \left(\frac{a}{D}\right)^2, \quad (10)$$

which is the analytic version of the phonon confinement model defined by Faraci *et al.*[52] In Eq. (10), $\Delta\omega(D)$ is the average shift of the peak position, D is the peak nanocrystal size, and a is the lattice constant ($a_{Si} = 0.543$ nm). Fig. 8(b) depicts the shift in the peak position and the peak size (inset) of small Si-NCs as a function of silane flow rate estimated after deconvolution of the raw data. As shown in this figure, the average sizes of small Si-NCs decrease from 5.4 to 3.8 nm with silane flow rate. For the flow rate of 4 sccs, the peak Si-NC size is estimated about 4.0 nm. This result is in close agreement with the average size estimated from TEM analyses. The volume fraction of small Si-NCs is estimated from the ratio of deconvoluted peak areas assigned to small and large Si-NCs. For Si-NCs synthesized with 4 sccs silane flow rate, the volume fraction is estimated as 60%, and in general, it is found to increase from 13% to 63% with silane flow rate. A comprehensive analysis of nanocrystal properties by using Raman spectroscopy will be reported in an upcoming article.

D. Photoluminescence spectroscopy

Photoluminescence spectroscopy is employed for further investigation of the size distribution and optical properties of Si-NCs. Size dependent luminescence from Si-NCs is observed when NCs are scaled-down to a size regime comparable to the exciton-Bohr radius ($r_{Si} \sim 4.9$ nm).[12,53,54] Fig. 9 presents PL spectra of Si-NCs synthesized with 4 sccs silane flow rate. The spectra are measured at multiple points from the central, ring, and outer regions (see Sec. III for detailed information) of the sample. As shown in Fig. 9, Si-NCs from different regions exhibit similar luminescence features in the visible region of the spectrum centered at 725 nm. The observed emission originates only from small Si-NCs. Large Si-NCs do not exhibit luminescence because of their lowered external quantum efficiency. In other words, large Si-NCs absorb significant amount of the excitation as a result of their large cross section; however, they release the absorbed energy in non-radiative ways, i.e., in the form of heat. The presence of large Si-NCs in the deposits does not modify the characteristic shape of the emission. However, it reduces the actual PL intensity originated from small Si-NCs because of re-absorption of the emitted luminescence. The size distribution as a function of band gap energy is defined as[55]

$$E(D) = E_{g,Si} + \frac{3.73}{D^{1.39}}, \quad (11)$$

where $E_{g,Si}$ is the band gap energy of bulk silicon crystal (1.1 eV), D is the average size of Si-NCs, and $E(D)$ is the size dependent band gap energy. The estimated size distributions from the different positions on the substrate are similar. Fig. 10 shows that the PL size distribution has a similar trend with TEM size distribution at smaller sizes. The observed deviation with increased size could be due to weakened confinement within the larger NCs and/or due to the defects that quench the luminescence from larger Si-NCs. Another possible reason for the observation of this deviation in the size distribution is the formation of an oxide shell on the surface of Si-NCs, which results in a decrease in the size of Si-NCs.

In the Introduction, it is mentioned that establishing a production technique that can reach scalable throughputs of Si-NCs with controlled material properties is essential for realization of devices based on Si-NCs. Our findings confirm that Si-NCs can be produced with ultrahigh throughputs by using a remote expanding thermal plasma technique. It is important to note that synthesized Si-NCs are free standing and it is possible to control the peak size of small Si-NCs by varying the silane flow rate. The results obtained from XRD, TEM, RS, and PL analyses suggest that small Si-NCs synthesized in the ETP have similar optical and morphological properties with respect to the Si-NCs synthesized in other techniques that provide good control on the material properties, however, with lower throughputs.[14,15] Observation of the bimodal size distribution is related with the significant differences in the residence times found in the plasma

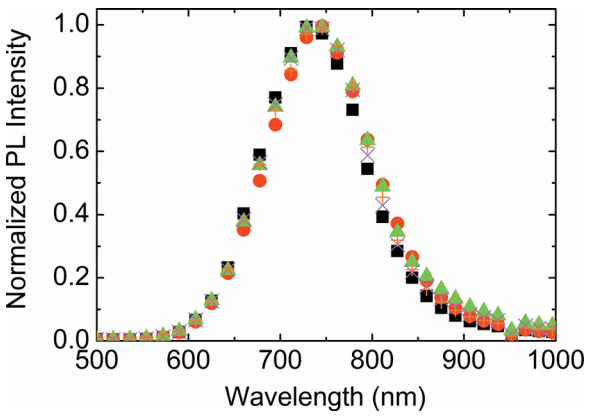

FIG. 9. PL spectra of small Si-NCs measured from various parts of the sample deposited with 4 sccs silane flow rate.

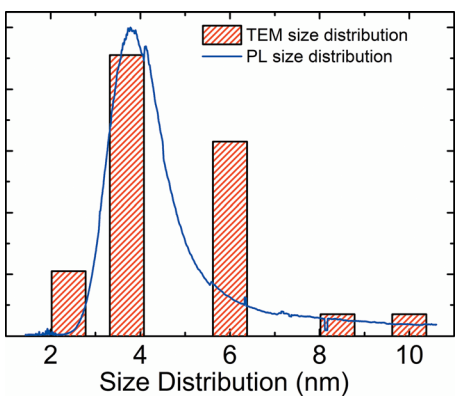

FIG. 10. Comparison of PL size distribution and TEM statistical size distribution for the sample deposited with 4 sccs silane flow rate.

regions concluding that small and large Si-NCs are synthesized in the central beam and recirculation cells, respectively. Moreover, as a result of diffusion and drag forces in both of these plasma regions, a lognormal size distribution is observed for small and large Si-NCs. TEM images show the presence of significantly larger Si-NCs with monocrystalline morphology implying that they are not the result of coalescence of smaller Si-NCs, i.e., large Si-NCs are formed from primary core clusters by means of nucleation of plasma species. If coalescence is considered as a possible formation mechanism for large Si-NCs, the coalescence of large particles (tens of nanometers) into larger particles (hundreds of nanometers) should be taken into account as well as the coalescence of small particles. In this case, inter-particle grain boundaries should be observed in the large Si-NCs as the recirculation cells do not have sufficient heat for triggering large particle coalescence. However, TEM images in Fig. 5 demonstrate that this is not the case for large Si-NCs, i.e., large Si-NCs have monocrystalline morphology. On the other hand, small Si-NCs synthesized in the central beam are observed as dendritic groups suggesting that the collision rate is faster than a possible coagulation rate, leaving the nucleation as the most favorable formation mechanism for Si-NCs. These observations are noteworthy in the sense that the particle formation in our system (and possibly in the systems where particle formation is strongly governed by drift and diffusion in a finite growth regime[25]) does not follow the commonly believed nucleation, agglomeration, coagulation sequence.

According to the indications of Raman spectroscopy, there is an inverse relation between the silane flow and the average size of small Si-NCs. Higher silane densities in the plasma beam increases the population of critical-sized clusters and promotes rapid nucleation which results in a rapid decrease of the nucleating species in the plasma beam due to the increased number of available sites on the surface of small clusters. Therefore, higher silane flows increases the volume fraction of small Si-NCs in the deposits and decreases their average size.

One of the main advantages of the ETP is the high throughput processing of Si-NCs with a rate of 100 mg/min, which is achieved in lab-scale conditions. The level of throughput achieved is dramatically higher when compared to other high-rate processing techniques. In comparison, a high rate laser pyrolysis method[56] and a non-thermal plasma method[15] are reported with throughputs up to 200 mg/h and 52 mg/h, respectively. When scaled up, the ETP can potentially reach significantly higher throughputs of Si-NCs. Generally, when all the process parameters are scaled up linearly, the level of throughput scales up with 1.5–2.0 mg $cm^{-2} min^{-1}$ as a function of surface area where the deposition takes place. Even though more than 90% of the silane is converted into Si-NCs, the practical efficiency is limited by the surface area of the deposited substrate. When the total mass of silane injected into downstream is considered for 5 sccs flow rate ($\sim$350 mg min^{-1}), the amount of throughput collected on a 4 in. diameter substrate (100 mg min^{-1}) is about 30% of the converted silane. Therefore, using larger substrates can further increase the practical efficiency.

For most of the technological applications, large Si-NCs are unwanted as their presence can detrimentally affect the unique size-dependent optical, electronic, and chemical properties of small Si-NCs and decrease the overall external quantum efficiency. Therefore, elimination of large Si-NCs is an important subject. Assuming small Si-NCs are formed in the plasma beam and large Si-NCs are formed in the recirculation cells, spatial isolation of recirculation cells can possibly prevent diffusion of small Si-NCs to these cells and potentially hinder the formation of large Si-NCs.

V. CONCLUDING REMARKS

Remote expanding thermal plasma is a scalable technique which brings along high throughput production of Si-NCs together with easy handling and average size control. The established throughput in the lab-scale conditions is about 100 mg/min which is promoted by utilizing high powers and high silane flow rates injected into downstream during synthesis. Plasma chemistry during nanoparticle synthesis is initiated only by Ar^+ ions as the electron temperature is not high enough for dissociation of silane molecules. All observed nanoparticles are monocrystalline and no evidence is found for coalescence of smaller nanocrystals into larger particles. The required heat for crystallization of nanoparticles is provided by abundant hydrogen abstraction and passivation reactions, and by dissociative adsorption of radicals and silane molecules. Residence time distribution in the plasma imposed by the flow field is an important parameter on the final size of Si-NCs. Among the analysis techniques, Raman spectroscopy is found to be the most useful technique as it reveals the morphology, size distribution, and average size of Si-NCs in a non-destructive and time efficient manner. Finally, the challenge relies on establishing a better control on the average size distribution of Si-NCs, which is a prerequisite for realistic future applications based on Si-NCs.

ACKNOWLEDGMENTS

This work is part of the research programme of the Foundation for Fundamental Research on Matter (FOM), which is part of the Netherlands Organisation for Scientific Research (NWO). Authors of this work thank M. J. F. van de Sande for skillful technical assistance.

[1]J. De la Torre, A. Souifi, A. Poncet, C. Busseret, M. Lemiti, G. Bremond, G. Guillot, O. Gonzalez, B. Garrido, J. R. Morante, and C. Bonafos, Physica E (Amsterdam) **16**, 326 (2003).
[2]L. B. Hu, H. Wu, S. S. Hong, L. F. Cui, J. R. McDonough, S. Bohy, and Y. Cui, Chem. Commun. (Cambridge) **47**, 367 (2011).
[3]A. Dana, I. Akca, O. Ergun, A. Aydinli, R. Turan, and T. G. Finstad, Physica E (Amsterdam) **38**, 94 (2007).
[4]G. Conibeer, M. Green, R. Corkish, Y. Cho, E. Cho, C. Jiang, T. Fangsuwannarak, E. Pink, Y. Huang, T. Puzzer, T. Trupke, B. Richards, A. Shalav, and K. Lin, Thin Solid Films **511–512**, 654 (2006).
[5]M. Zacharias, J. Heitmann, R. Scholz, U. Kahler, M. Schmidt, and J. Blasing, Appl. Phys. Lett. **80**, 661 (2002).
[6]I. Dogan, I. Yildiz, and R. Turan, Physica E (Amsterdam) **41**, 976 (2009).
[7]U. Serincan, G. Aygun, and R. Turan, J. Lumin. **113**, 229 (2005).
[8]T. Shimizu-Iwayama, N. Kurumado, D. E. Hole, and P. D. Townsend, J. Appl. Phys. **83**, 6018 (1998).
[9]J. P. Wilcoxon, G. A. Samara, and P. N. Provencio, Phys. Rev. B **60**, 2704 (1999).

[10]R. K. Baldwin, K. A. Pettigrew, J. C. Garno, P. P. Power, G. Y. Liu, and S. M. Kauzlarich, J. Am. Chem. Soc. **124**, 1150 (2002).
[11]J. D. Holmes, K. J. Ziegler, R. C. Doty, L. E. Pell, K. P. Johnston, and B. A. Korgel, J. Am. Chem. Soc. **123**, 3743 (2001).
[12]G. Ledoux, J. Gong, F. Huisken, O. Guillois, and C. Reynaud, Appl. Phys. Lett. **80**, 4834 (2002).
[13]X. G. Li, Y. Q. He, and M. T. Swihart, Langmuir **20**, 4720 (2004).
[14]R. Gresback, T. Nozaki, and K. Okazaki, Nanotechnology **22**, 305605 (2011).
[15]L. Mangolini, E. Thimsen, and U. Kortshagen, Nano Lett. **5**, 655 (2005).
[16]B. N. Jariwala, O. S. Dewey, P. Stradins, C. V. Ciobanu, and S. Agarwal, ACS Appl. Mater. Interfaces **3**, 3033 (2011).
[17]R. W. Liptak, B. Devetter, J. H. Thomas, U. Kortshagen, and S. A. Campbell, Nanotechnology **20**, 035603 (2009).
[18]M. C. M. van de Sanden and J. A. Tobin, Plasma Sources Sci. Technol. **7**, 28 (1998).
[19]W. M. M. Kessels, R. J. Severens, A. H. M. Smets, B. A. Korevaar, G. J. Adriaenssens, D. C. Schram, and M. C. M. van de Sanden, J. Appl. Phys. **89**, 2404 (2001).
[20]J. Hong, W. M. M. Kessels, F. J. H. van Assche, H. C. Rieffe, W. J. Soppe, A. W. Weeber, and M. C. M. van de Sanden, Prog. Photovoltaics **11**, 125 (2003).
[21]W. M. M. Kessels, C. M. Leewis, A. Leroux, M. C. M. van de Sanden, and D. C. Schram, J. Vac. Sci. Technol. A **17**, 1531 (1999).
[22]P. R. I. Cabarrocas, T. Nguyen-Tran, Y. Djeridane, A. Abramov, E. Johnson, and G. Patriarche, J. Phys. D: Appl. Phys. **40**, 2258 (2007).
[23]L. Mangolini and U. Kortshagen, Phys. Rev. E **79**, 026405 (2009).
[24]J. Perrin, O. Leroy, and M. C. Bordage, Contrib. Plasma Phys. **36**, 3 (1996).
[25]J. Söderlund, L. B. Kiss, G. A. Niklasson, and C. G. Granqvist, Phys. Rev. Lett. **80**, 2386 (1998).
[26]N. P. Rao, N. Tymiak, J. Blum, A. Neuman, H. J. Lee, S. L. Girshick, P. H. McMurry, and J. Heberlein, J. Aerosol Sci. **29**, 707 (1998).
[27]A. Bouchoule, A. Plain, L. Boufendi, J. P. Blondeau, and C. Laure, J. Appl. Phys. **70**, 1991 (1991).
[28]T. Kakeya, K. Koga, M. Shiratani, Y. Watanabe, and M. Kondo, Thin Solid Films **506–507**, 288 (2006).
[29]L. Boufendi, M. C. Jouanny, E. Kovacevic, J. Berndt, and M. Mikikian, J. Phys. D: Appl. Phys. **44**, 174035 (2011).
[30]R. Gresback, Z. Holman, and U. Kortshagen, Appl. Phys. Lett. **91**, 093119 (2007).
[31]N. Rao, S. Girshick, J. Heberlein, P. Mcmurry, S. Jones, D. Hansen, and B. Micheel, Plasma Chem. Plasma Process. **15**, 581 (1995).
[32]U. Kortshagen and U. Bhandarkar, Phys. Rev. E **60**, 887 (1999).
[33]U. Kortshagen, J. Phys. D: Appl. Phys. **42**, 113001 (2009).
[34]A. A. Fridman, L. Boufendi, T. Hbid, B. V. Potapkin, and A. Bouchoule, J. Appl. Phys. **79**, 1303 (1996).
[35]K. De Bleecker, A. Bogaerts, W. Goedheer, and R. Gijbels, IEEE Trans. Plasma Sci. **32**, 691 (2004).
[36]S. J. Choi and M. J. Kushner, J. Appl. Phys. **74**, 853 (1993).
[37]S. E. Selezneva, M. I. Boulos, M. C. M. van de Sanden, R. Engeln, and D. C. Schram, J. Phys. D: Appl. Phys. **35**, 1362 (2002).
[38]W. M. M. Kessels, C. M. Leewis, M. C. M. van de Sanden, and D. C. Schram, J. Appl. Phys. **86**, 4029 (1999).
[39]W. M. M. Kessels, M. C. M. van de Sanden, and D. C. Schram, Appl. Phys. Lett. **72**, 2397 (1998).
[40]E. Srinivasan, H. Yang, and G. N. Parsons, J. Chem. Phys. **105**, 5467 (1996).
[41]A. Bouchoule and L. Boufendi, Plasma Sources Sci. Technol. **2**, 204 (1993).
[42]C. G. Granqvist and R. A. Buhrman, J. Appl. Phys. **47**, 2200 (1976).
[43]B. R. Tull, J. E. Carey, M. A. Sheehy, C. Friend, and E. Mazur, Appl. Phys. A: Mater. Sci. Process. **83**, 341 (2006).
[44]J. J. Beulens, M. J. de Graaf, and D. C. Schram, Plasma Sources Sci. Technol. **2**, 180 (1993).
[45]M. C. M. van de Sanden, J. M. de Regt, and D. C. Schram, Plasma Sources Sci. Technol. **3**, 501 (1994).
[46]C. M. Hessel, J. Wei, D. Reid, H. Fujii, M. C. Downer, and B. A. Korgel, J. Phys. Chem. Lett. **3**, 1089 (2012).
[47]D. Comedi, O. H. Y. Zalloum, E. A. Irving, J. Wojcik, T. Roschuk, M. J. Flynn, and P. Mascher, J. Appl. Phys. **99**, 023518 (2006).
[48]A. L. Patterson, Phys. Rev. **56**, 978 (1939).
[49]W. W. Ke, X. Feng, and Y. D. Huang, J. Appl. Phys. **109**, 083526 (2011).
[50]I. H. Campbell and P. M. Fauchet, Solid State Commun. **58**, 739 (1986).
[51]C. C. Yang and S. Li, J. Phys. Chem. B **112**, 14193 (2008).
[52]G. Faraci, S. Gibilisco, P. Russo, A. R. Pennisi, and S. La Rosa, Phys. Rev. B **73**, 033307 (2006).
[53]W. D. A. M. De Boer, D. Timmerman, K. Dohnalova, I. N. Yassievich, H. Zhang, W. J. Buma, and T. Gregorkiewicz, Nat. Nanotechnol. **5**, 878 (2010).
[54]M. Sykora, L. Mangolini, R. D. Schaller, U. Kortshagen, D. Jurbergs, and V. I. Klimov, Phys. Rev. Lett. **100**, 067401 (2008).
[55]C. Delerue, G. Allan, and M. Lannoo, Phys. Rev. B **48**, 11024 (1993).
[56]X. Li, Y. He, S. S. Talukdar, and M. T. Swihart, Langmuir **19**, 8490 (2003).